

MANUSCRIPT

for publication in the

Journal of Power Sources

**In Operando Visualization of Hydride-Graphite Composites
during Cyclic Hydrogenation by High-Resolution
Neutron Imaging**

Carsten Pohlmann^a, Kai Herbrig^b, Łukasz Gondek^c, Nikolay Kardjilov^d,
André Hilger^d, Henryk Figiel^c, John Banhart^{d,e}, Bernd Kieback^{a,b},
Ingo Manke^d and Lars Röntzsch^{a,*}

^a *Fraunhofer Institute for Manufacturing Technology and Advanced Materials (IFAM),
Branch Lab Dresden, Winterbergstraße 28, 01277 Dresden, Germany*

^b *Technical University Dresden, Institute for Materials Science,
Helmholtzstraße 7, 01069 Dresden, Germany*

^c *AGH University of Science and Technology, Faculty of Physics and Applied Computer
Science, al. A. Mickiewicza 30, 30-059 Krakow, Poland*

^d *Helmholtz Center Berlin for Materials and Energy, Hahn-Meitner-Platz 1,
14109 Berlin, Germany*

^e *Technical University Berlin, Department of Materials Science and Technology,
Hardenbergstraße 36, 10623 Berlin, Germany*

*corresponding author: phone: +49-351-2537-411; fax: +49-351-2537-399

e-mail: Lars.Roentzsch@ifam-dd.fraunhofer.de

Research Highlights:

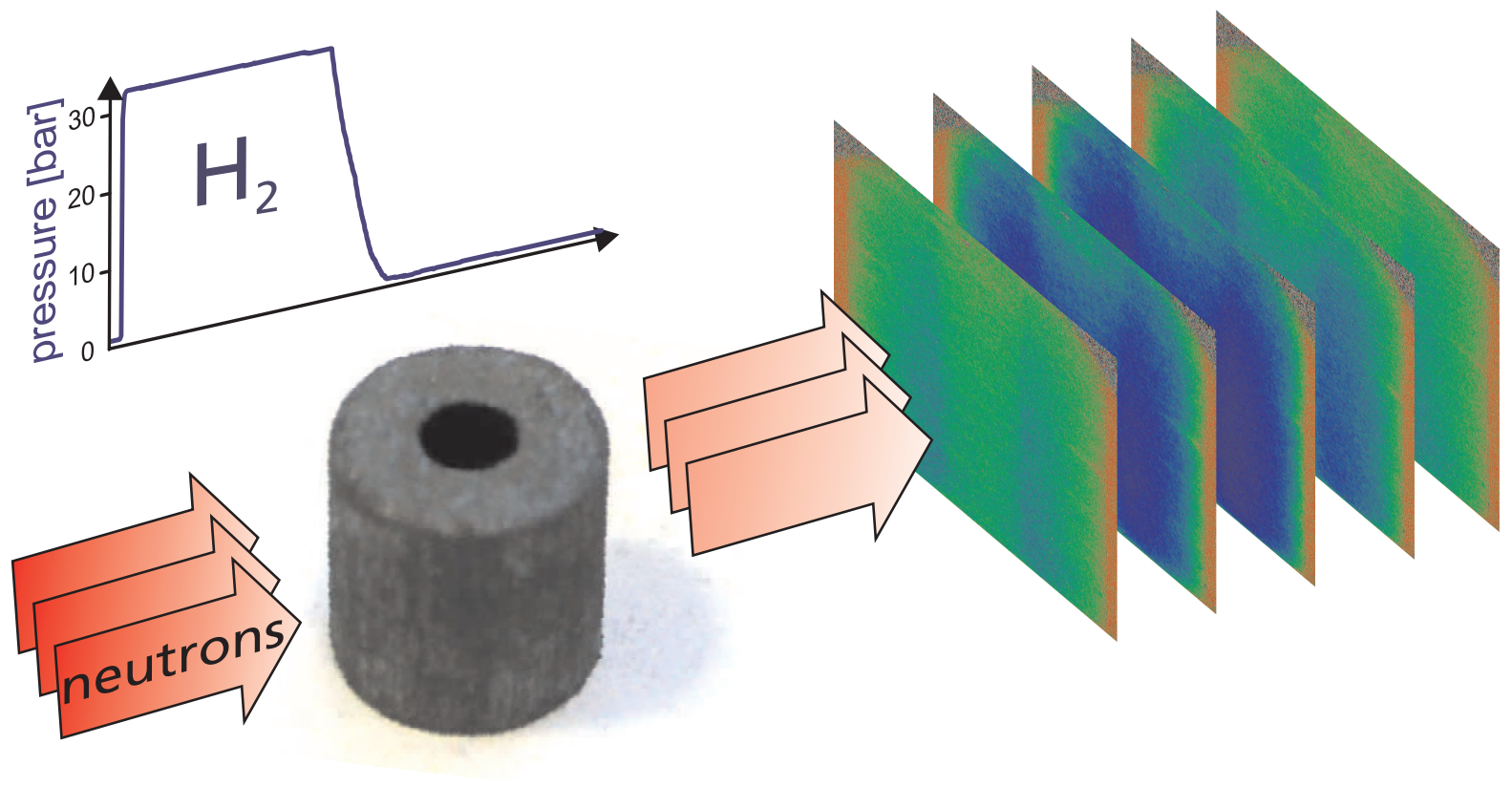
- Hydrogenation of hydride-graphite composites (HGC) is visualized *in operando* by neutron imaging
- Unexpected activation of HGCs through formation of active regions is examined
- Reaction fronts inside HGCs are visualized for the first time
- Fast loading and unloading of HGC with hydrogen is realized (< 1 minute)

Abstract

Hydrogen solid-state storage in metal hydrides has attracted remarkable attention within the past decades due to their high volumetric storage densities at low operating pressures. In particular, recently emerged hydride-graphite composites (HGC) can enable a safe, reliable and very compact hydrogen storage solution for various applications. In this regard, only little is known about the activation behavior of such HGC, their cycle stability and degradation effects. Because of the high sensitivity to hydrogen, neutron imaging offers a distinctive approach to examine *in operando* reaction fronts, swelling effects and microstructural changes of hydrogen absorbing materials with high spatial and temporal resolution. In this contribution, a comprehensive analysis of various phenomena during activation and cycling of HGC based on a Ti-Mn hydrogen absorbing alloy and expanded natural graphite is reported for the first time. A neutron radiography and tomography set-up with a spatial resolution down to 7 μm was utilized allowing highest detection precision. During initial hydrogenation, regions with enhanced reactivity are observed which contradicts a theoretically expected homogeneous reactivity inside the HGC. These active regions grow with the number of hydrogenation-dehydrogenation cycles until the whole HGC volume uniformly participates in the hydrogen sorption reaction. With regard to long-term hydrogenation-dehydrogenation cycling, inhomogeneous swelling effects were observed from which essential conclusions for technical HGC-based tank systems can be derived.

Keywords

High-resolution neutron imaging; hydride-graphite composite; AB₂ hydrogen absorbing alloy; gas and heat transfer; volume swelling



1 Introduction

Renewable energy sources are gaining importance, which is why the development of environmentally friendly energy storage and energy distribution technologies is essential [1-3]. In this respect, hydrogen is a clean, safe and carbon-free energy carrier for portable, mobile as well as stationary applications [4-9]. A hydrogen-based energy cycle demands for efficient, compact and safe storage solutions [10]. Due to high hydrogen storage capacities and moderate operating pressures, metal hydrides have increasingly attracted attention within recent years [11-14].

Although a large number of hydride-forming metallic alloys is known [15, 16], only a few are in commercial use, for example La-Ni, Ti-Mn and some Mg alloys [17-19]. In this contribution, an AB₂-type Ti-Mn alloy (also called Hydralloy[®] C5₂) was used which is already in commercial application, for example, for maritime fuel cell applications [18]. Hydralloy[®] C5₂ has a gravimetric hydrogen storage capacity of about 1.8 wt.-%-H₂ [20] at room temperature combined with a high volumetric hydrogen storage capacity up to 100 g-H₂·l⁻¹ [21]. Hydralloy[®] C5₂ can be classified as room-temperature hydrogen storage material because it can be hydrogenated from -20°C to +60°C at moderate hydrogen pressures. Moreover, it exhibits very fast intrinsic sorption kinetics [22, 23]. Thus, Hydralloy[®] C5₂ is also suitable for thermochemical applications such as non-mechanical hydrogen compressors or actuators where fast system dynamics are needed [24, 25]. A further promising application is the thermochemical storage of industrial heat where a Hydralloy[®]-based solid-bed reactor can be coupled to a high-temperature hydride reactor (e.g. based on MgH₂) to store the hydrogen generated during heat excess times and to release it on demand to rehydrogenate the high-temperature hydride [26, 27].

Besides the intrinsic hydrogen sorption kinetics of the storage material, the loading and unloading dynamics of hydride-based storage tanks are further influenced by the heat and gas

transport properties of the hydride bed. From the viewpoint of realistic hydride tank systems, the transfer of the reaction heat through the hydride bed is usually the rate-determining step, because loose powder beds are known for inferior heat transfer properties, which is a serious drawback for numerous applications [28, 29]. In order to overcome this limitation hydride-graphite composites (HGC) were developed recently. These composite materials exhibit an increased effective thermal conductivity and higher mechanical stability, which, thereby, facilitate handling during fabrication and a markedly improved (un-)loading dynamics of the storage tank. According to the literature, two major routes can provide enhanced heat conduction in a hydride bed. One approach is to embed the hydrogen absorbing alloy in auxiliary metal structures of high thermal conductivity, for example nickel or aluminum fins or open-cellular foams [30-32]. The second approach focuses on composites of hydrogen absorbing alloys and graphite [33-38]. Following this path, the thermal conductivity can be tailored very accurately. In addition, anisotropic heat conduction and strongly increased volumetric storage capacities compared to those of loose powders can be realized using uniaxial compaction techniques. In our previous works [36, 37, 39, 40] we demonstrated that compacted composites of MgH_2 , $NaAlH_4$, $LiNH_2$ and Hydralloy[®] with graphite have superior effective thermal conductivities in the radial direction, which is beneficial when using a cylindrical geometry of the storage compartment. Moreover, the residual porosity of such HGC can be adjusted to meet the requirements of the storage container concerning gas permeability, mechanical stability and geometrical integrity during cycling.

With regard to Hydralloy[®]-based HGC [40], it was found that during the first hydrogenation-dehydrogenation cycles the hydrogen sorption kinetics as well as the hydrogen storage capacity improve continuously. Furthermore, a change of physical properties such as gas permeability and thermal conductivity with the number of hydrogenation-dehydrogenation cycles was observed. Up to now, it is not clear what causes this behavior and how it affects

the long-term performance of the HGC. Since Hydralloy[®] dehydrogenates at room temperature and atmospheric pressure it is not possible to investigate the properties of HGC in their hydrogenated state outside a reactor. Thus, an *in operando* method of visualization of HGC during cyclic hydrogenation accompanied by a mapping of the hydrogen element distribution inside the HGC can contribute to a better understanding of the hydrogenation behavior of HGC. In turn, such results would allow us to draw conclusions on materials production and HGC-based storage tank design.

In this contribution, the behavior of HGC based on Hydralloy[®] and expanded natural graphite (ENG) concerning their initial hydrogenation cycles in combination with an activation procedure is discussed. In this regard, neutron imaging (radiography and tomography) was used to examine HGC during hydrogenation and dehydrogenation. In contrast to X-rays, neutrons are suitable to investigate processes inside hydrogen absorbing materials [41]. In principle, the attenuation of the neutron beam passing through an object is described by the Lambert-Beer law:

$$I = I_0 e^{-\Sigma d} \quad (1)$$

where I_0 is an incident beam intensity, Σ is the linear attenuation coefficient and d is the thickness of the irradiated sample. Σ depends on the corresponding scattering and absorption cross-sections and on the density of the scattering centers. For neutrons, Σ is not related to the atomic number of the element in a simple and monotonic way as for X-rays, but depends on the internal structure of the nucleus of the atom under study. Hydrogen nuclei exhibit one of the largest cross-sections among the elements. This provides excellent contrast between hydrogen and common metals such as Al, Ni, Cu etc. For this reason, containers made of aluminum are almost “transparent” for a neutron beam (even for a wall thickness exceeding

10 mm). In addition, Hydralloy[®] (Ti-Zr-Mn-V-Fe alloy) and graphite are quite transparent to the neutron beam as well.

In our previous work [42] it was reported that hydrogenation of a loose metal hydride powder bed can be examined utilizing neutron imaging. It was possible to visualize a hydrogenation front moving through the powdery reaction bed. Furthermore, it was found that the hydrogenation proceeds faster close to the containers walls, which indicates the necessity of adequate heat removal from the hydride bed during hydrogen uptake. Here we discuss the behavior of Hydralloy[®]-based HGC during initial hydrogenation and inhomogeneous swelling effects during long-term cycling for the first time.

2 Experimental

Hydralloy[®] C5₂ (51 wt.% Mn, 28 wt.% Ti, 14 wt.% V, 3 wt.% Fe, 3 wt.% Zr) was purchased from *GfE Metalle und Materialien GmbH*. The material was delivered as 2 mm to 10 mm large granules that were powderized through milling for 5 min under argon to prevent unwanted oxidation. After this, the powder was blended with 5 wt.% ENG. **This mixture was then compacted** at 75 MPa into cylindrical solid bodies (pellets) of 12 mm diameter. These parameters were chosen according to our previous work [40]. Subsequently, an axial hole of 4 mm in diameter was drilled (cf. Fig. 1). All processing steps were performed under inert atmosphere following the processing chain described in our previous work [40]. All investigated HGC were inserted into aluminum alloy containers (cf. Fig. 2 inset) and submitted to an activation procedure. During this activation, the samples were exposed to elevated temperatures (ca. 125°C) at varying pressures of 1 h in vacuum and 2 h at 5 bar hydrogen (99.9999% purity) repeated four times.

The neutron imaging experiments were conducted *in-operando* at beam line CONRAD (V7) of the research reactor BERII at the Helmholtz Center Berlin for Materials and Energy in Germany (HZB). The cold neutron instrument was equipped with a high-resolution detector [43, 44]. Cold neutrons (low energy) offer better contrast than thermal neutrons due to a higher attenuation. The incident neutron beam has a broad approximately Maxwellian spectrum including wavelengths from about 0.09 nm to 1.0 nm with maximum flux at 0.25 nm. The sample was mounted on a goniometric table enabling rotation and translation around two axes. To ensure a good heat transfer between the container and the ambience, the outer container walls were subjected to a flow of pressurized air at room temperature. The scintillating screen ($\text{Gd}_2\text{O}_2\text{S}$) of about 14 mm diameter and a thickness of 10 μm is used to convert neutrons to visible light. It was placed in closest proximity behind the sample. Thus, a very high spatial resolution was achieved with one pixel representing an area of $6.4 \times 6.4 \mu\text{m}^2$. The light generated in the scintillator is reflected by a mirror into the focusing optical system and guided to the Andor DW436N-BV CCD camera allowing a 2048×2048 resolution. The CCD camera was cooled by Peltier elements to -50°C in order to keep spurious signals at the lowest possible level. The exposure times used for the experiments ranged from 5 s to 20 s for each radiographic projection image. Figure 2 depicts the set-up used for high-resolution neutron imaging.

Before starting each experiment, a dark field image (DFI) and a flat field image (FFI) were recorded. DFIs were recorded with the neutron beam stopped in order to observe the dark currents in the CCD camera. FFIs were collected to record the distribution of the neutron beam without the sample. The difference between FFI–DFI can be attributed directly to the incident beam intensity (I_0 in Eq. 1). In analogy, after subtracting the DFI from the image of the investigated sample, the image can be interpreted as the transmitted beam intensity (I in Eq. 1). By dividing these two corrected images (I/I_0) and knowing the path length of the

neutron beam through the sample (thickness d), the attenuation coefficient (Σ) can be calculated. In radiographic images, the obtained information is still integrated along the path of the neutrons within the sample.

The hydrogenation/dehydrogenation cycles were controlled manually. For the investigation of the initial cycles after activation the hydrogen pressure was increased to 30 bar quasi-instantaneously and kept at this level for at least 1.5 min. For subsequent dehydrogenation the pressure was decreased to 1 bar (absolute) with a constant hydrogen flow of $100 \text{ l}\cdot\text{h}^{-1}$ (normalized) using a manually controlled flow regulator. The according pressure cycles are depicted in Figure 3. During this procedure neutron images (20 s exposure time) were taken only at 30 bar and 1 bar pressure. Thus, pictures of the either fully hydrogenated or dehydrogenated states were obtained. After an almost constant hydrogenation performance was established, the HGC was also examined concerning its hydrogen uptake and release behavior by continuously taking images with 5 s exposure time. Therefore, the hydrogenation and dehydrogenation was resolved dynamically.

For tomography, three radiographic images (each with 20 s exposure time) per angle increment of 0.3° were acquired with a total rotation of 180° . The three images were processed by a median filter in order to obtain a projection image with better signal-to-noise parameters. These 600 projection images were used for the reconstruction of the three-dimensional (3D) distribution of the attenuation coefficient which actually represents the 3D structure of the HGC.

Taking the logarithm of normalized image data, I/I_0 in Eq. (1), yields Σd or $\Sigma' \rho d$, where $\Sigma' = (\Sigma/\rho)$ is the mass-specific attenuation coefficient characteristic for each element and neutron wavelength spectrum. The integral over a volume of interest (VOI) within an image yields $\Sigma' m$, where m is the total mass in the volume. Therefore, m can be calculated once the mass attenuation coefficient is known. For an appropriate VOI it can be assumed that only

hydrogen enters and leaves the VOI during hydrogenation or dehydrogenation. A change in the integral value is, therefore, directly related to a change of the total mass of hydrogen within the VOI. Hydrogen is present within the VOI either in gaseous form or chemically bound in the hydride. Since the mass of the HGC is known the average hydrogen concentration of the HGC can be calculated. The mass attenuation coefficient of hydrogen was determined by measuring the neutron transmission of water filled into a same sample container. The contribution of oxygen to the total attenuation compared to that of hydrogen can be neglected. As a result $33 \text{ cm}^2/\text{g}$ for the mass attenuation coefficient, which corresponds to a cross section of 55 barn of a single hydrogen nuclei (110 barn for molecular hydrogen), was used in the following evaluation. For the given energy spectrum of the incident neutrons (0.0008 eV to 0.1 eV, peak at 0.013 eV) the literature (ENDF/B-VII.1 database [45]) reports a cross-section of 23 barn to 132 barn. Hence, the experimentally obtained value is reasonable. The predominant interaction of neutrons with hydrogen ^1H nuclei gives strongly incoherent scattering with an almost homogenous spherical angular distribution of the scattered neutrons. Due to the finite distance between the sample and the detector, the scintillator will capture some of the scattered neutrons. Thus, one would get an apparently lower attenuation compared to an infinite detector distance. Consequently, the measured attenuation coefficient depends on the geometric configuration of the setup and should be understood as an effective mass attenuation coefficient of hydrogen for the specific wavelength spectrum and geometric setup.

3 Results and discussion

As described in our previous work the Hydralloy[®]-based HGC do not exhibit the full hydrogen capacity and (un-)loading dynamics right after the activation procedure [40]. It was shown that both values increase significantly within the first hydrogenation-dehydrogenation cycles after activation. The number of cycles necessary to achieve full performance strongly depends on the activation temperature and duration. Furthermore, the cycling temperature and hydrogenation pressure also influence the evolution of performance. In order to improve the activation procedure for industrial applications where shortest durations and lowest temperatures are preferred, it is of utmost interest to investigate what is happening within the first cycles inside the HGC. The following section is dedicated to the examination of the first cycles using high-resolution neutron radiography. The activation procedure was carried out prior to the neutron experiments. After that, the long-term hydrogenation and dehydrogenation properties of such HGC are focused in a separate section. In order to realize a sufficient thermal conductivity and gas permeability of the examined HGC, an ENG content of 5 wt.% and a compaction pressure of 75 MPa is chosen as described previously [40, 46].

3.1 Initial hydrogenation cycles after the activation procedure

The activation procedure resembles a heat treatment of the HGC under hydrogen without significant hydrogen uptake aiming at generating fresh metallic surfaces that readily absorb hydrogen. Activated Hydralloy[®]-based HGC indeed instantly absorb hydrogen but the hydrogenation kinetics as well as the total hydrogen capacity still increase within the first complete hydrogenation-dehydrogenation cycles until constant sorption properties are reached [40].

In order to investigate how the hydrogen uptake of the HGC proceeds within the first hydrogenation-dehydrogenation cycles, sequenced imaging was performed at hydrogen pressures of 30 bar and 1 bar during hydrogenation and dehydrogenation, respectively (cf. Fig. 3). The hydrogen content was determined by means of the integral value of attenuation of the according neutron images as stated above.

During these cycles, two phases with a gradual transition can be identified: In the first phase, a strong increase in absorbed hydrogen with each further hydrogenation step is observed. This increase is accompanied by an increase/decrease in the maximum/minimum temperature during hydrogenation and dehydrogenation since a larger volume fraction of the HGC participates in the reaction (growing heat source or heat sink strength of the exothermic and endothermic reaction, respectively). Furthermore, the total amount of residual hydrogen that remains within the sample after dehydrogenation increases. This correlates to the increasing fraction of material participating in the hydrogenation and, thus, to the absorbed hydrogen which then cannot be released completely at a hydrogen pressure of about 1 bar during dehydrogenation. **Since most of HGC becomes activated during these cycles it is denoted as the 'activation phase'.**

In the second phase, the entire HGC volume participates in the hydrogenation reaction. Yet, there is still a slow increase in hydrogen capacity with increasing cycle number. Unlike expected, a slight decrease in the amount of hydrogen remaining in the sample during dehydrogenation is examined. This effect can be explained by the fact that from around the 25th cycle minor amounts of the HGC are pushed outside of the field of view (cf. Fig. 4) and, therefore, cannot be evaluated as described above. Regarding the development of the temperature peaks there is only a minor increase in activation within phase two. From a technological point of view, constant hydrogen sorption properties can be defined at the end of phase one. **Therefore, in the following the HGC is considered as activated with a**

sufficiently stable hydrogenation performance. This allows evaluating the cycling performance of the HGC at different operation conditions (see next section).

In Figure 4, an intense macroscopic swelling of the HGC during cyclic hydrogenation can be observed. Starting from the initial as-compacted and as-activated state, the HGC increases in volume. This is related to the swelling of the lattice of the hydrogen-absorbing alloy during hydrogenation. The swelling effect is not homogeneous and clear differences along the sample axis are observed. At the top, where free space is available, the HGC expands significantly more. In Figure 1, slices from a tomogram in the vertical and horizontal planes of a cycled HGC are shown. From the vertical slice, it can be deduced that the upper part of the HGC is much less dense and has larger cracks than the bottom. The horizontal slice shows a homogenous density distribution with no cracks at the bottom of the HGC. The resolution is high enough to dissolve even single “veins” of ENG, which allows for microstructural investigations.

After the first phase, less pronounced changes in the shape of the HGC occur and an almost constant sample height is observed during radiography. There is still a difference between the hydrogenated and the dehydrogenated state, which can be understood as “breathing” of the HGC. This “breathing” does not reflect the whole volume expansion expected from the lattice expansion of the hydrogen-absorbing alloy inside the HGC since it can be partially compensated by the intrinsic porosity of the HGC. Furthermore, the diameter of the central hole used for axial hydrogen transport decreases, which is also caused by the above mentioned swelling effects. Hence, it is advisable to integrate a stabilizing distribution pipe (e.g. porous sinter tube) for application engineering.

For radiographic evaluation, the region to be examined quantitatively in Figure 4 was chosen at the bottom of the HGC where the change in material density during cycling is less pronounced, which limits the errors in the determination of the hydrogen concentration.

A selection of radiographic images of the hydrogenated state after various cycle numbers is depicted in Figure 5 (also see online video data: Video_Data_to_Fig5_(Activation).avi). All images represent the relative change in attenuation at end of the hydrogen pressure build-up and, thus, refer to the fully hydrogenated state of each cycle. Higher attenuation corresponds to a higher hydrogen concentration in the specific area. All pictures represent an integral value of the attenuation and hydrogen concentration along the path of the neutrons through the cylindrical HGC, which can be simplified to a chord of a circle. After the first hydrogenation step no notable hydrogen concentration can be observed inside the HGC. The largest part of the hydrogen is stored as gas pressurized to 30 bar inside the open pores of the HGC and the free volume inside the test tank. Starting with the fifth hydrogenation cycle, a hydrogen absorbing region inside the HGC can be noticed (marked by a red cycle in Figure 5).

Here, hydrogenation takes place while the surrounding volume still does not participate in the hydrogen uptake. With each following cycle this and other active regions grow in size. We suspect that due to a local temperature increase during the exothermic hydrogenation reaction neighboring volumes of the region are activated. Such activation might be understood as the formation of small cracks in the native oxide surface layers of the hydrogen-absorbing particles inside the HGC. These cracks can result from stresses, which are due to differences in the respective thermal expansion coefficients and/or lattice expansion effects caused by the hydrogenation itself (also puncturing of neighboring particles). Additionally, due to the locally increased temperature hydrogen might diffuse faster through the oxide layer. The local heat production increases with the size of the active region, which allows for a faster growth of the region with progressing cycling.

It is assumed, that these active regions appear statistically distributed within the HGC. A locally high packing density of the storage material particles (related to a higher heat source density), the crack density of the oxide layers and/or the local heat transfer properties (e.g.

distance to a graphite vein inside the HGC) might influence the occurrence of active regions. These regions increase in size until the whole HGC participates in hydrogen uptake and release. At the end of this process, a largely homogeneous hydrogen distribution is observed in the HGCs hydrogenated state.

This is the first time that the formation of such active regions in HGC is reported to play a key role in the overall activation behavior of such hydrogen storage materials. The hydrogen capacity of the HGC increases continuously afterward, but at a different pace. The increase in capacity is accompanied by a steady volume swelling of the HGC.

3.2 Hydrogenation performance at a constant hydrogen capacity

In this section, two different sets of sorption cycles are examined. After the intense cycling of the HGC (45 cycles), it is assumed that the HGC is fully activated and a constant hydrogenation capacity and performance is achieved. At this stage, the entire volume of the HGC participates in hydrogen sorption and about 1.4 wt.% of hydrogen can be stored reversibly. In the following, the reference point for hydrogen capacity is the low hydrogen level after dehydrogenation in the last cycle depicted in Figure 3. To investigate the propagation of potential hydrogenation fronts through the HGC, two cycles were conducted with different pressure increase and decrease rates for hydrogenation and dehydrogenation, respectively.

First, a cycle comprising fast hydrogenation and slow dehydrogenation was carried out. Figure 6 depicts selected radiographic images at different times throughout this cycle (compare online video data: Video_Data_to_Fig6_(fast_Hydrogenation).avi). The exposure time of each picture is 5 s and, therefore, each picture represents the hydrogen concentration averaged over this time interval. The images (1)–(3) depict stages during hydrogenation,

image (4) shows the distribution of hydrogen in the hydrogenated state and images (5)–(8) were taken during dehydrogenation.

Figure 7 (a) illustrates the temperature and pressure development as well as the amount of hydrogen absorbed during this cycle. The times are marked at which the images of Figure 6 were taken. The hydrogen profiles across the six images in Figure 6 are depicted in Figure 7 (b). During hydrogenation, the formation of the hydride phase starts from the outside of the HGC where the heat of reaction can be dissipated fastest. Apparently, the transport of hydrogen related to the gas permeability of the HGC is not rate limiting.

To calculate the hydrogen concentration it is mandatory to normalize the images to the local HGC thickness, i.e. the pathway of the neutrons travelling through the HGC (dividing by the according thickness, i.e. the length of the chord). The thickness changes along the diameter of the HGC. For the inner part of the HGC, the thickness consists of a pathway through the composite material as well as a pathway through the pressurized gas volume in the center of the HGC (central hole). Since the concentration of hydrogen in the gas volume is significantly lower compared to the hydride, the attenuation of the gas within the hole is neglected, which, however, results in a small error of hydrogen content especially at 30 bar. This effect can be observed in Figures 6 and 7 (b) where the central part of the HGC seems to have higher hydrogen concentrations, which in fact is due to pressurized hydrogen gas in the hole. During dehydrogenation, this effect is less pronounced since the hydrogen gas pressure is significantly lower.

While releasing hydrogen from the HGC slowly, the hydrogen content follows time-delayed and much more rapidly. Once the equilibrium pressure is passed the dehydrogenation starts immediately. Due to a high heat transfer at the walls of the reactor, a faster decrease in hydrogen concentration is achieved there.

In the next experiment, a cycle comprising a slow hydrogenation and a fast dehydrogenation step was investigated. Figure 8 depicts selected radiographic images at different times throughout this cycle where the hydrogen concentration is mapped (also compare online video data: Video_Data_to_Fig8_(slow_Hydrogenation).avi). In analogy to Figure 6, the images (1)–(3) depict stages during hydrogenation, image (4) shows the distribution of hydrogen in the hydrogenated state and images (5)–(8) are taken during dehydrogenation. Figure 9 illustrates the temperature and pressure development, the amount of hydrogen being absorbed and the cross-sectional distribution of the images (in analogy to Fig. 7).

In contrast to fast hydrogenation, a much more homogeneous hydrogen concentration is detected during a slow pressure increase. The misleading higher concentration in the concentric hole is notable, the reasons of which are explained above. A sufficient heat transfer with respect to the heat generation rate is achieved. This is also reflected in the broadened temperature peak. An additional decrease in pressure build up would further smoothen the temperature peak and result in an even more homogeneous hydrogen distribution.

During the fast dehydrogenation, a similar behavior of the hydrogen distribution compared to the slow dehydrogenation is observed. By comparing the time-span of both dehydrogenations, it is obvious that in both cases three pictures can be taken while most of the hydrogen is released. Yet, the start of hydrogen release during the fast pressure decrease is more abrupt, which is also reflected in a sharper temperature peak. There might be differences in the hydrogen distribution between both cases, which, however, cannot be distinguished here.

In summary, during fast (un-)loading the reaction fronts are strongly influenced by the heat transfer inside the reaction bed. Thus, the reaction proceeds from the walls of the container towards the center of the HGC. At low reaction rates the heat generation rate is low, which allows for a sufficient heat transfer throughout the reaction bed and results in a homogeneous

hydrogen concentration development. At this point it is unclear how the structural integrity of the HGC is influenced by these (un-)loading parameters. It seems reasonable that fast rates can cause high gas pressures and expansion differences in the HGC, which might lead to a pronounced deterioration of the HGC. These phenomena will be studied in more detail in the future.

4 Conclusion

A unique experimental set-up for neutron imaging was utilized to examine the activation behavior and the cycling performance of HGC based on a Ti-Mn alloy with expanded natural graphite. Prior to the *in operando* neutron investigations, the HGC were exposed to an activation pretreatment at 125°C under a low pressure hydrogen atmosphere (≤ 5 bar) where no hydrogenation occurs. After this pretreatment, some hydrogenation-dehydrogenation cycles are needed until the full hydrogen capacity as well as the hydrogen sorption kinetics are reached [40]. These first cycles were examined by *in operando* neutron imaging:

- Active regions inside the HGC appear statistically distributed, whereas the remaining HGC volume stays inactive.
- These active regions grow with the number of cycles, most likely due to locally increased temperatures that enable the activation of neighboring volumes.
- In the final state, the active regions have spread over the whole HGC volume, which marks the end of the activation.
- The growth of the active regions is accompanied by an increase in the overall swelling of the HGC.
- During this first phase, the degree of volume expansion of the HGC increases continuously. This expansion originates from the lattice expansion of the hydrogen

absorbing material during hydrogenation. However, it is partly compensated by the intrinsic porosity of the HGC.

- In phase two, the overall expansion is not further increasing significantly. Yet, there is a difference between the hydrogenated and dehydrogenated state, which can be referred to axial “breathing” of the HGC.

In the second part of this investigation, the (de-)hydrogenation of fully activated HGC is discussed. A fast and a slow hydrogenation and dehydrogenation was observed using neutron radiography:

- During a fast reaction triggered by applying and releasing hydrogen pressure almost instantly, reaction fronts are clearly visible inside the HGC. They start at the container wall where the heat transfer is fastest. The gas transfer is obviously not rate-determining.
- At slow hydrogenation rates, a very homogeneously distributed hydrogen concentration increase can be observed. In this case, the heat transfer is sufficiently fast to ensure hydrogenation requirements throughout the whole HGC volume.
- Very fast loading and unloading dynamics can be achieved (< 1 minute).

In summary, it was possible to visualize the formation and growth of active regions in HGC for the first time. They play a key role in achieving a fully activated state. Future investigations will focus on the influence of different (de-)hydrogenation rates and on size effects on the HGC swelling.

5 Acknowledgement

This work was partly funded by the Friedrich-und-Elisabeth-Boysen-Stiftung and by the BMBF (Federal Ministry of Education and Research of Germany; contract no. 03EK3020A), all of which is gratefully acknowledged. Furthermore, the authors would like to thank the

excellent experimental support granted by the staff of the Helmholtz Center Berlin for Materials and Energy.

References

- [1] J.-F. Hake, J. Linssen, M. Walbeck, *Energ. Policy* 34 (2006) 1271- 1283.
- [2] U. Büsgen, W. Dürschmidt, *Energ. Policy* 37 (2009) 2536- 2545.
- [3] J. Andrews, B. Shabani, *Int. J. Hydrogen Energ.* 37 (2012) 1184-1203.
- [4] M. Momirlan, T.N. Veziroglu, *Int. J. Hydrogen Energ.* 30 (2005) 795-802.
- [5] M.T. Gencoglu, Z. Ural, *Int. J. Hydrogen Energ.* 34 (2009) 5242-5248.
- [6] W. Dougherty, S. Kartha, C. Rajan, M. Lazarus, A. Bailie, B. Runkle, A. Fencl, *Energ. Policy* 37 (2009) 56-67.
- [7] P. Meibom, K. Karlsson, *Int. J. Hydrogen Energ.* 35 (2010) 1853-1863.
- [8] C. Darras, M. Muselli, P. Poggi, C. Voyant, J.-C. Hoguet, F. Montignac, *Int. J. Hydrogen Energ.* (2012).
- [9] Enertrag, *Fuel Cells Bull.* 2012 (2012) 14.
- [10] G. Principi, F. Agresti, A. Maddalena, S.L. Russo, *Energy* 34 (2009) 2087.
- [11] L. Schlapbach, A. Züttel, *Nature* 414 (2001) 353-358.
- [12] A. Züttel, *Mater. Today* 6 (2003) 24-33.
- [13] P. Moriarty, D. Honnery, *Int. J. Hydrogen Energ.* 32 (2007) 1616-1624.
- [14] E.M. Gray, C.J. Webb, J. Andrews, B. Shabani, P.J. Tsai, S.L. Chan, *Int. J. Hydrogen Energ.* 36 (2011) 654-663.

- [15] U. Eberle, G. Arnold, R.v. Helmolt, J. Power Sources 154 (2006) 456-460.
- [16] B. Sakintuna, F. Lamari-Darkrim, M. Hirscher, Int. J. Hydrogen Energ. 32 (2007) 1121-1140.
- [17] D. Linden, T.B. Reddy, Handbook of batteries, McGraw-Hill, 2002.
- [18] U. Eberle, M. Felderhoff, F. Schüth, Angew. Chem. Int. Ed. 48 (2009) 6608-6630.
- [19] M. Jehan, D. Fruchart, J. Alloy Compd. 580, Supplement 1 (2013) S343-S348.
- [20] GfE, Hydralloy[®] Data Sheet (2012).
- [21] D. Fruchart, J.L. Soubeyroux, R. Hempelmann, J. Less Common Met. 99 (1984) 307-319.
- [22] V.M. Skripnyuk, M. Ron, Int. J. Hydrogen Energ. 28 (2003) 303-309.
- [23] M.T. Hagström, P.D. Lund, J.P. Vanhanen, Int. J. Hydrogen Energ. 20 (1995) 897-909.
- [24] M.T. Hagström, J.P. Vanhanen, P.D. Lund, J. Alloy Compd. 269 (1998) 288-293.
- [25] Z. Dehouche, N. Grimard, F. Laurencelle, J. Goyette, T.K. Bose, J. Alloy Compd. 399 (2005) 224-236.
- [26] M. Felderhoff, B. Bogdanovic, Int. J. Mol. Sci. 10 (2009) 325-344.
- [27] D.N. Harries, M. Paskevicius, D.A. Sheppard, T.E. Price, C.E. Buckley, Proceedings of the IEEE 100 (2012) 539-549.
- [28] D.K. Ross, Vacuum 80 (2006) 1084-1089.

- [29] J. Zhang, T.S. Fisher, P.V. Ramachandran, J.P. Gore, I. Mudawar, *J. Heat Transf.* 127 (2005) 1391-1399.
- [30] F. Laurencelle, J. Goyette, *Int. J. Hydrogen Energ.* 32 (2007) 2957-2964.
- [31] S. Mellouli, H. Dhaou, F. Askri, A. Jemni, S.B. Nasrallah, *Int. J. Hydrogen Energ.* 34 (2009) 9393-9401.
- [32] H. Wang, A.K. Prasad, S.G. Advani, *Int. J. Hydrogen Energ.* 37 (2012) 290-298.
- [33] A.R. Sánchez, H.-P. Klein, M. Groll, *Int. J. Hydrogen Energ.* 28 (2003) 515-527.
- [34] H.-P. Klein, M. Groll, *Int. J. Hydrogen Energ.* 29 (2004) 1503-1511.
- [35] A. Chaise, P.d. Rango, P. Marty, D. Fruchart, S. Miraglia, R. Olivès, S. Garrier, *Int. J. Hydrogen Energ.* 34 (2009) 8589-8596.
- [36] C. Pohlmann, L. Röntzsch, S. Kalinichenka, T. Hutsch, B. Kieback, *Int. J. Hydrogen Energ.* 35 (2010) 12829-12836.
- [37] C. Pohlmann, L. Röntzsch, S. Kalinichenka, T. Hutsch, T. Weißgärber, B. Kieback, *J. Alloy Compd.* 509, Supplement 2 (2011) S625-S628.
- [38] B.v. Hassel, D. Mosher, J.M. Pasini, M. Gorbounov, J. Holowczak, X. Tang, R. Brown, B. Laube, L. Pryor, *Int. J. Hydrogen Energ.* 37 (2012) 2756-2766.
- [39] C. Pohlmann, L. Röntzsch, J. Hu, T. Weißgärber, B. Kieback, M. Fichtner, *J. Power Sources* 205 (2012) 173-179.
- [40] C. Pohlmann, L. Röntzsch, F. Heubner, T. Weißgärber, B. Kieback, *J. Power Sources* 231 (2013) 97-105.

- [41] J. Banhart, A. Borbély, K. Dzieciol, F. Garcia-Moreno, I. Manke, N. Kardjilov, A.R. Kaysser-Pyzalla, M. Strobl, W. Treimer, *International Journal of Materials Research* 101 (2010) 1069-1079.
- [42] Ł. Gondek, N.B. Selvaraj, J. Czub, H. Figiel, D. Chapelle, N. Kardjilov, A. Hilger, I. Manke, *Int. J. Hydrogen Energ.* 36 (2011) 9751-9757.
- [43] N. Kardjilov, A. Hilger, I. Manke, M. Strobl, M. Dawson, S. Williams, J. Banhart, *Nuclear Instruments and Methods in Physics Research Section A: Accelerators, Spectrometers, Detectors and Associated Equipment* 651 (2011) 47-52.
- [44] N. Kardjilov, A. Hilger, I. Manke, M. Strobl, M. Dawson, J. Banhart, *Neutron News* 20 (2009), 20-23.
- [45] G.M. Hale, *Nuclear Data for Science and Technology ENDF/B-VII.1 MAT 125* (2006).
- [46] C. Pohlmann, L. Röntzsch, T. Weißgärber, B. Kieback, *Int. J. Hydrogen Energ.* 38 (2013) 1685-1691.

Figure Captions

Fig. 1: Hydralloy®-based hydride-graphite composite (HGC) containing 5 wt.% expanded natural graphite compacted at 75 MPa. The horizontal and vertical slices were obtained by neutron tomography of the HGC after 35 (de-)hydrogenation cycles.

Fig. 2: Schematic drawing of the experimental set-up for the neutron imaging experiments on the hydride-graphite composites.

Fig. 3: Stored hydrogen content, temperature response and hydrogen pressure during the initial cycles after activation. The calculated amount of hydrogen was based on the measured neutron transmission.

Fig. 4: Neutron radiography of a Hydralloy®-based hydride-graphite composite with 5 wt.% expanded natural graphite in its initial state, after 25 and 45 hydrogenation cycles (dehydrogenated state). The section examined is highlighted.

Fig. 5: Development of the relative change in attenuation in the hydrogenated state within the first 45 cycles after activation (examination section is depicted in Figure 4).

Fig. 6: Hydrogen concentration during fast hydrogenation (instant pressure build-up) and slow dehydrogenation (within ~1 min). The time span in which each picture was acquired is depicted. A corresponding pressure-temperature-plot is given in Figure 7 (examination section depicted in Figure 4).

Fig. 7: (a) Pressure and temperature course and corresponding hydrogen content. Dots on the latter curve represent neutron images taken *in operando*, vertical lines mark the numbered images given in Figure 6. (b) Hydrogen profile across the diameter of the HGC at the six selected times given by the vertical lines in (a).

Fig. 8: Hydrogen concentration development during slow hydrogenation (within approx. 2.7 min) and fast dehydrogenation (instant pressure drop). The time span in which each picture was acquired is depicted. According pressure-temperature-plot is given in Figure 9 (examination section depicted in Figure 4).

Fig. 9: (a) Pressure and temperature course and corresponding hydrogen content. Dots on the latter curve represent neutron images taken *in operando*, vertical lines mark the numbered images given in Figure 8. (b) Hydrogen profile across the diameter of the HGC at the six selected times given by the vertical lines in (a).

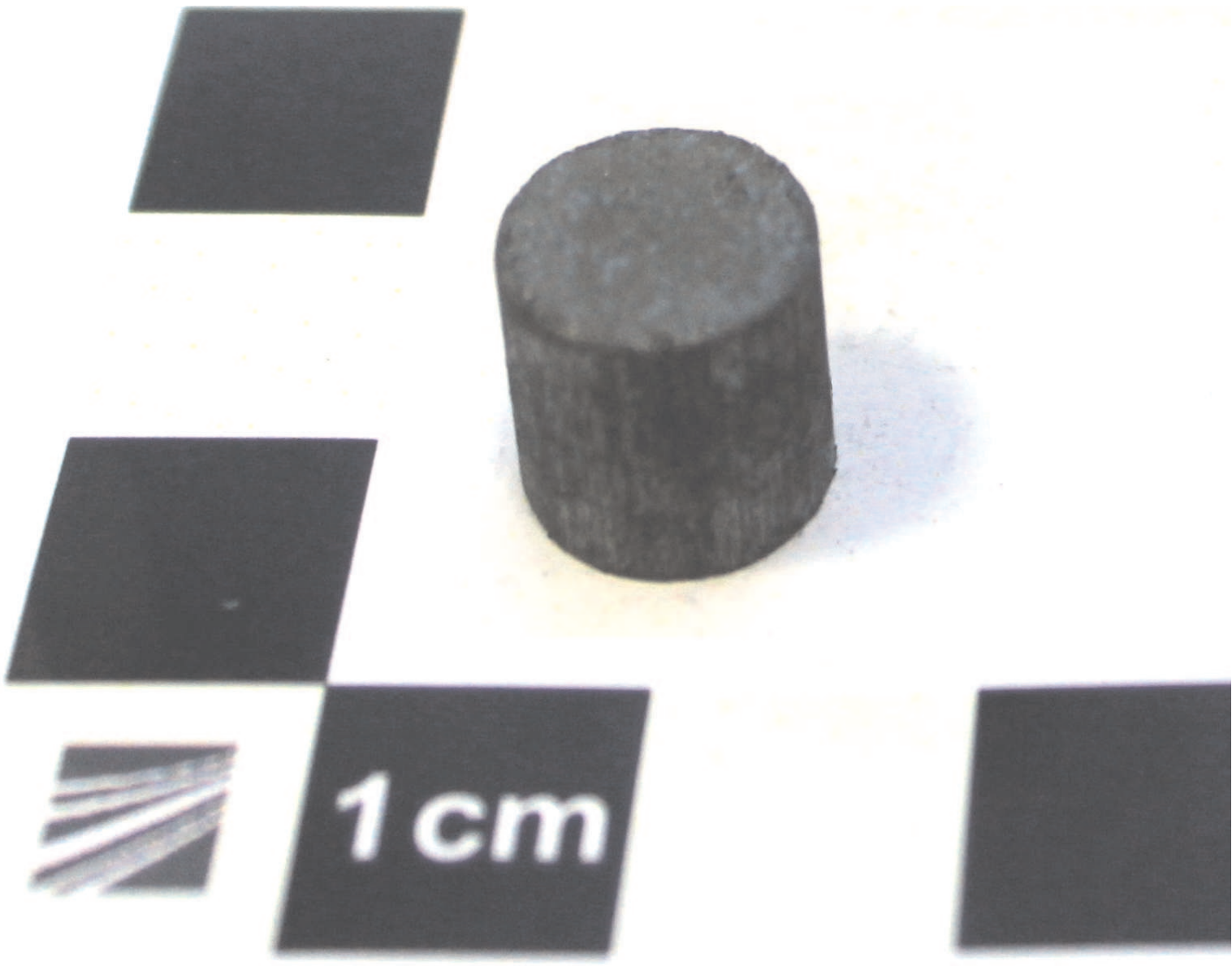


Figure2

[Click here to download Figure\(s\): Fig_2.eps](#)

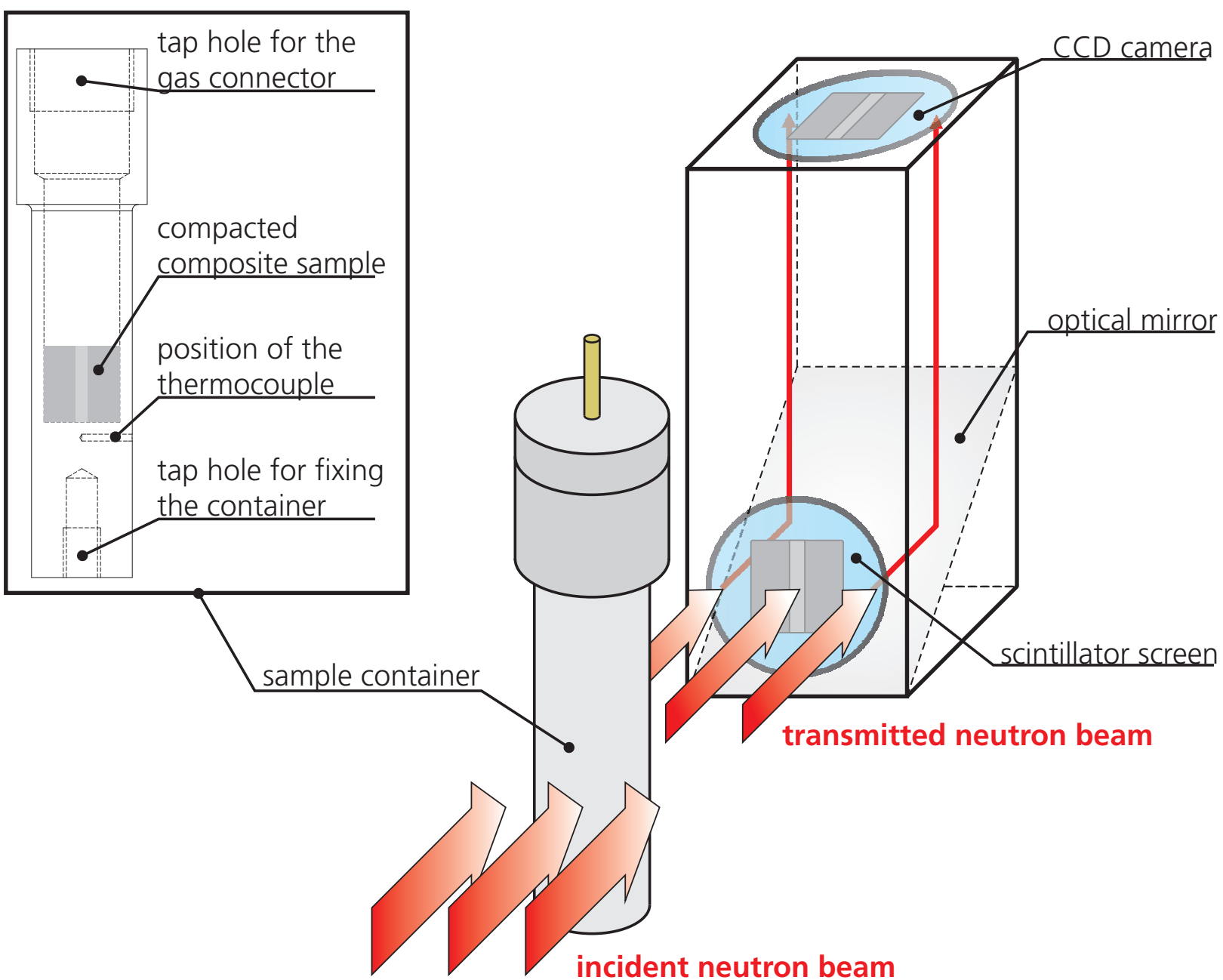


Figure3

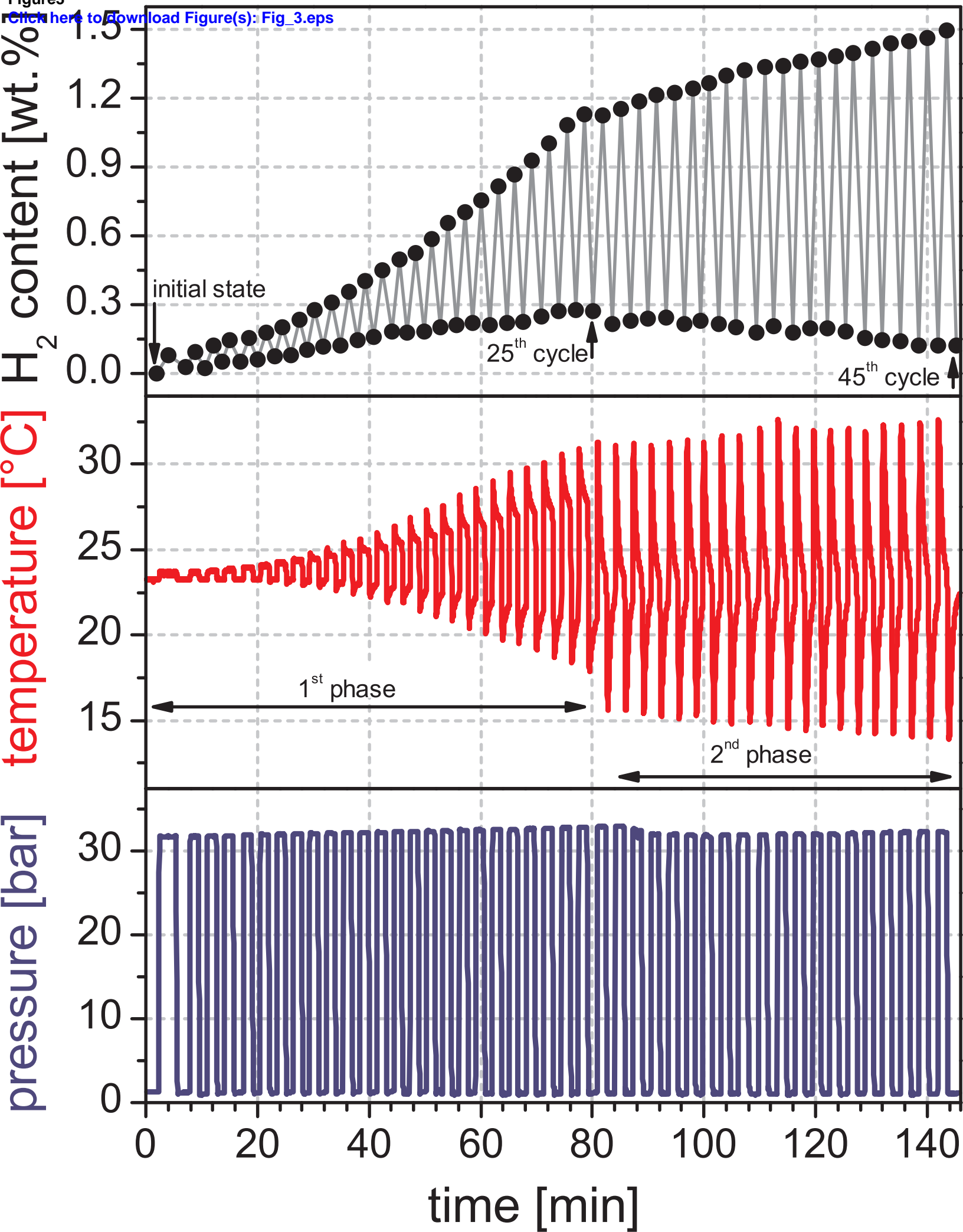
[Click here to download Figure\(s\): Fig_3.eps](#)

Figure4

[Click here to download Figure\(s\): Fig_4.eps](#)

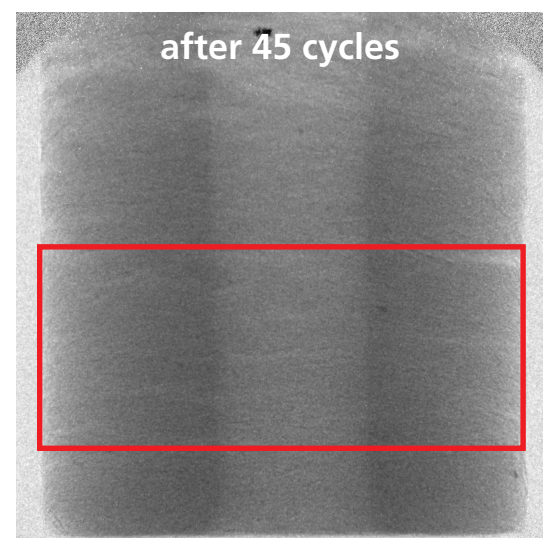
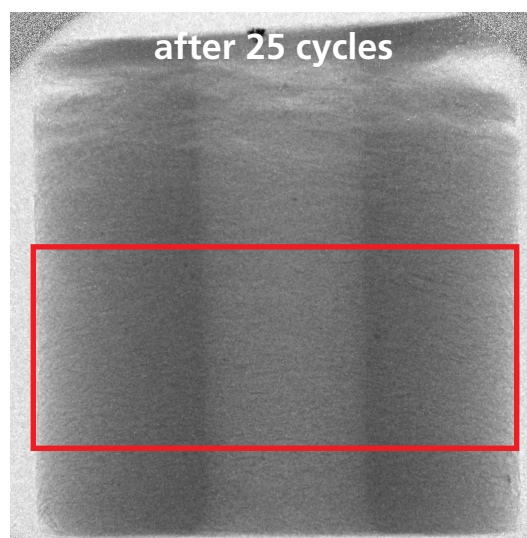
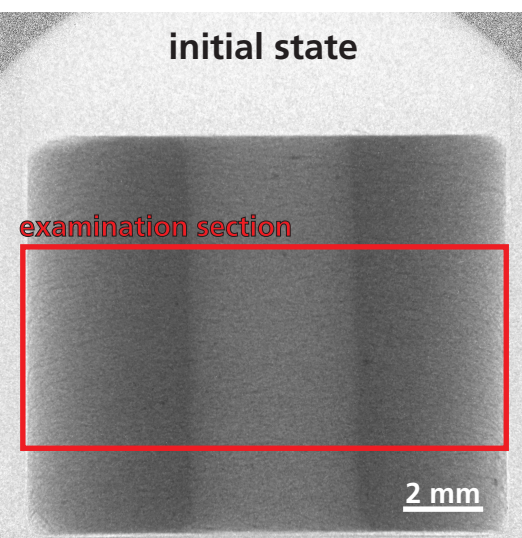


Figure5

[Click here to download high resolution image](#)

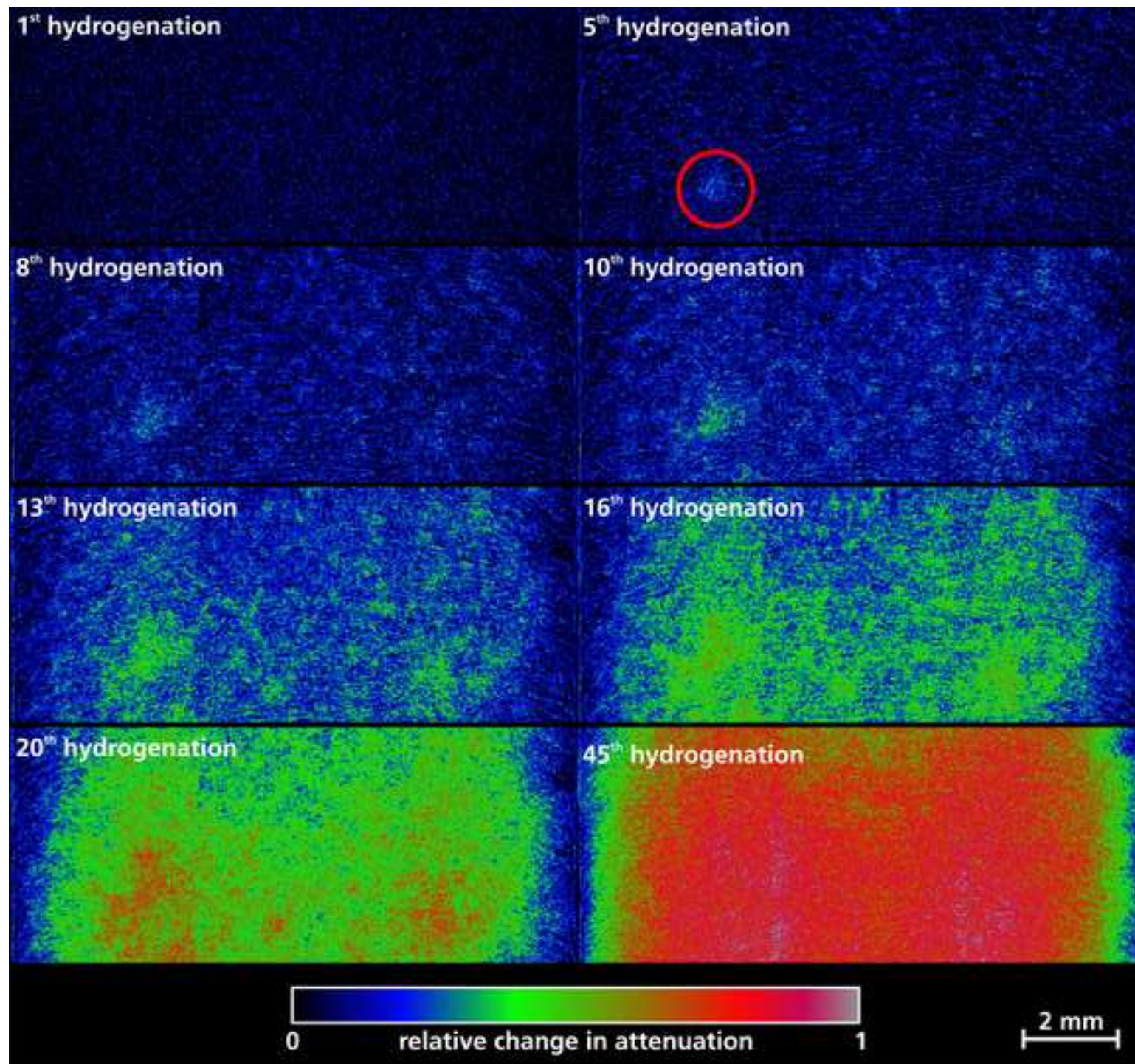


Figure6

[Click here to download high resolution image](#)

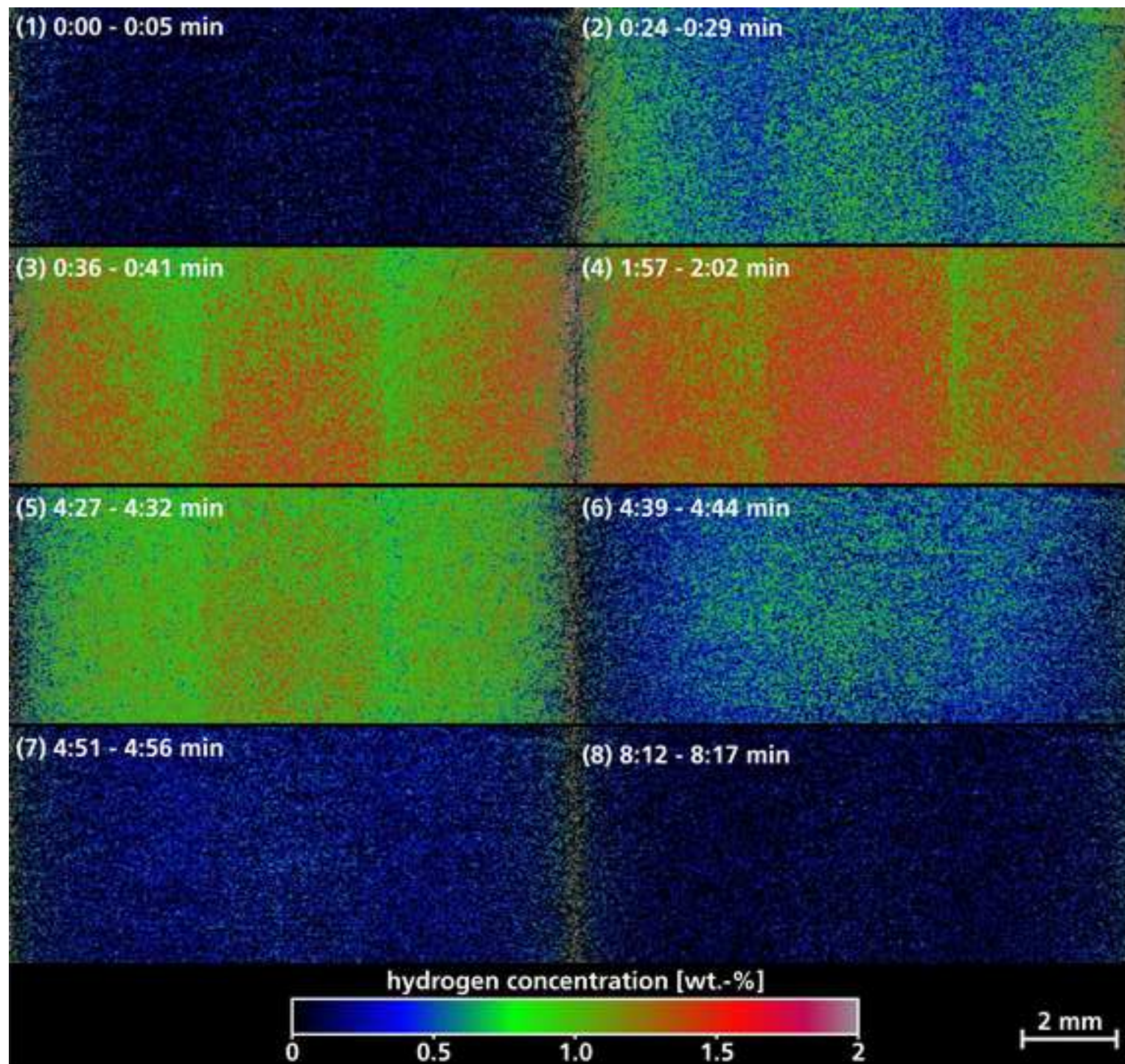


Figure7

[Click here to download Figure\(s\): Fig_7.eps](#)

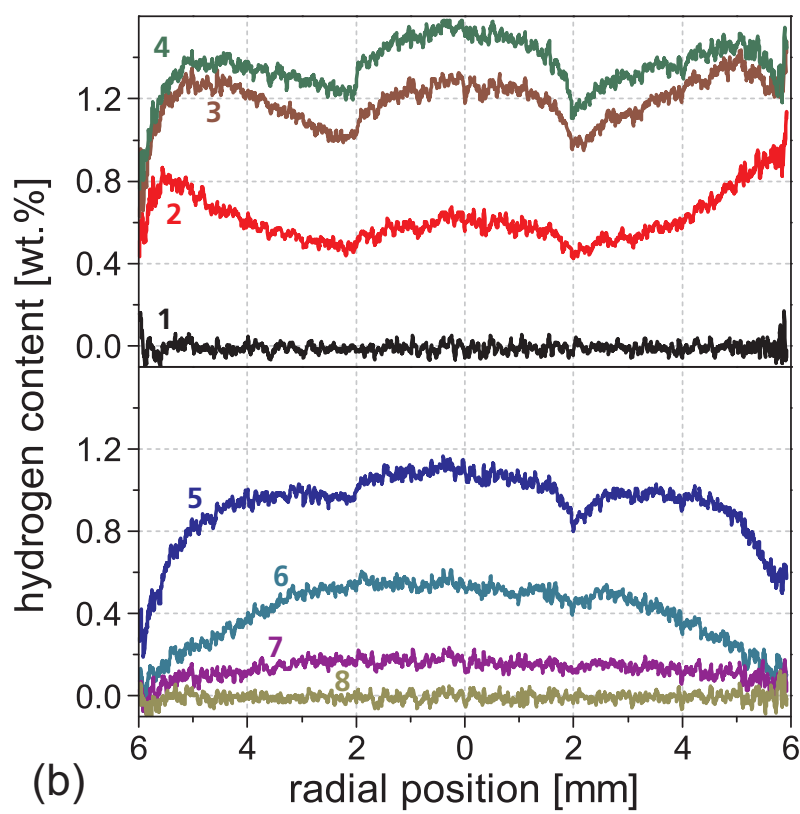
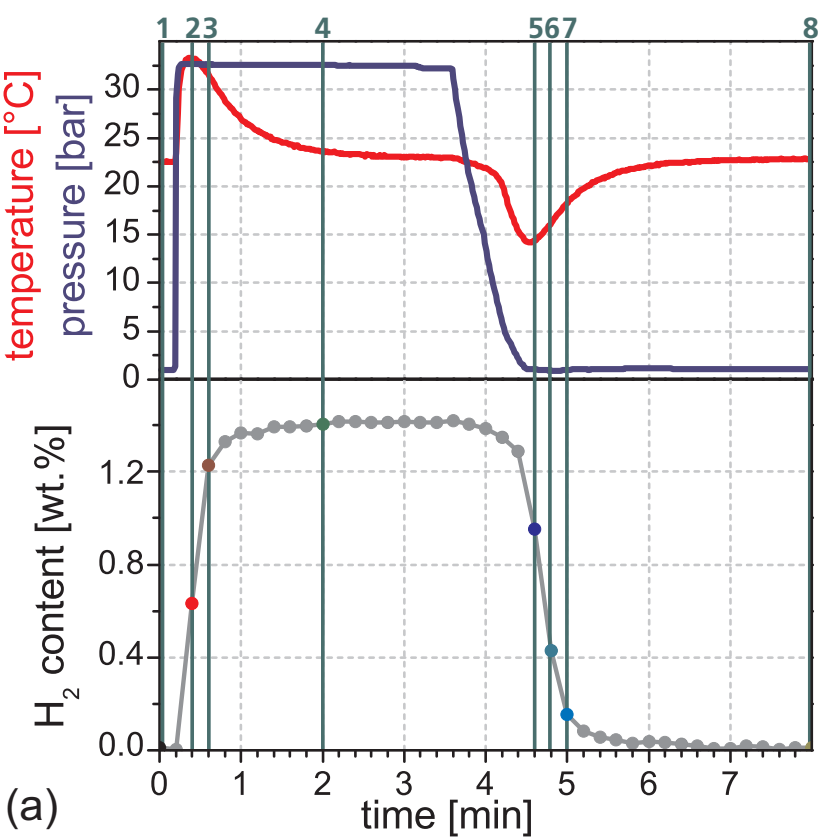


Figure8

[Click here to download high resolution image](#)

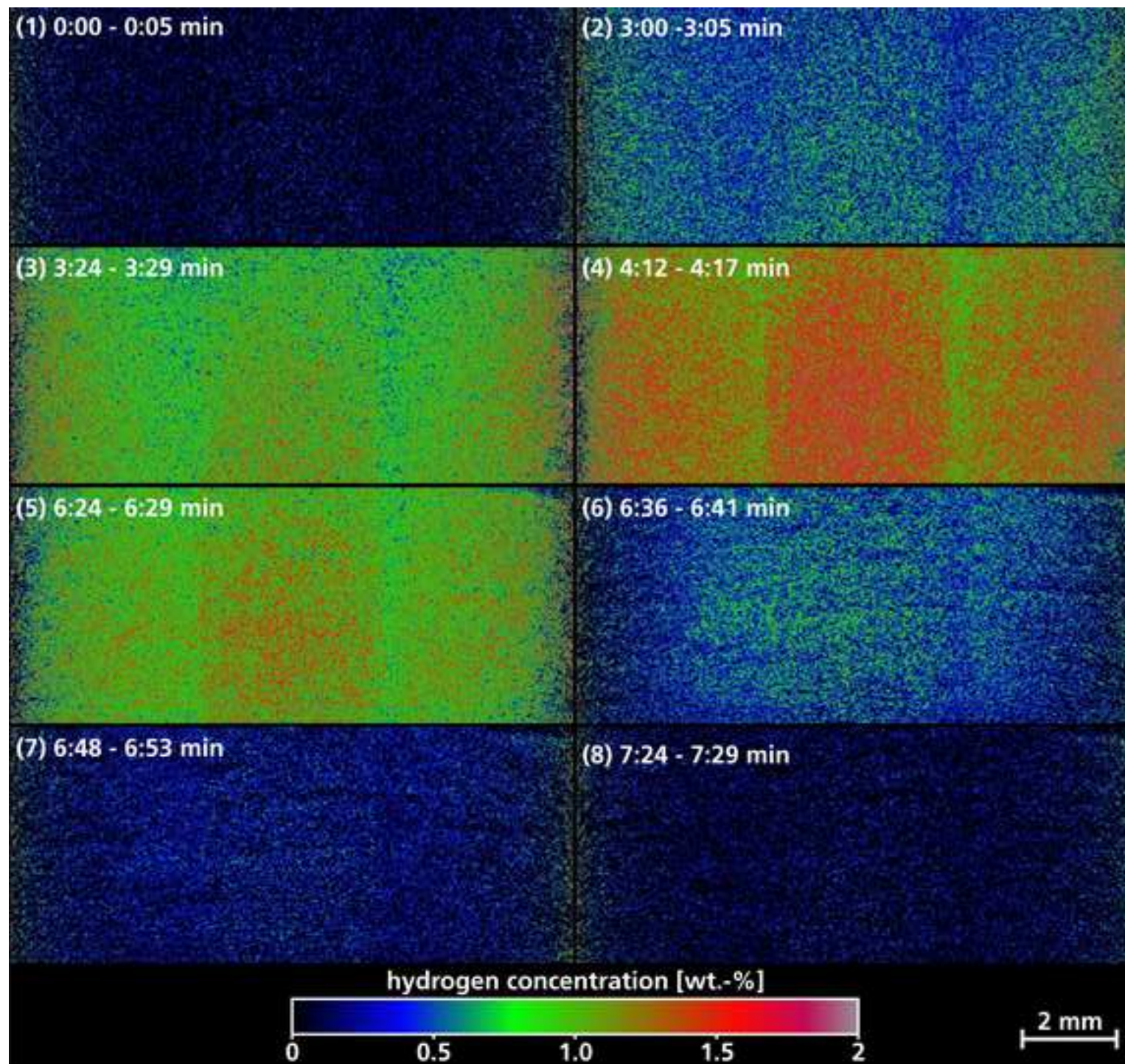


Figure9

[Click here to download Figure\(s\): Fig_9.eps](#)